predicted abundance ratios for all stable r-process elements in a neighbouring range of mass numbers should be identical to those observed in the star and in the Solar System[4,16]. The accuracy of a predicted ratio depends both on the adopted nuclear physics model and on the degree to which different production sites yield similar results. The latter has generally been found to be the case for previously studied r-process enhanced stars, but further work is needed to verify it in detail for CS31082–001.

Both theoretical and observational uncertainties should be minimal for elements as close as possible to each other in atomic number. Thus, Os and Ir should be the best stable reference elements in CS31082–001 for the radioactive species ^{232}Th and ^{238}U (any ^{235}U has decayed to insignificance long ago). From the half-lives of ^{232}Th and ^{238}U (14.05 and 4.468 Gyr, respectively), Δt as a function of the logarithmic decay of Th and U is:

$$\Delta t = 46.7[\log(\mathrm{Th}/r)_0 - \log(\mathrm{Th}/r)_{\mathrm{obs}}] \quad (1)$$

$$\Delta t = 14.8[\log(\mathrm{U}/r)_0 - \log(\mathrm{U}/r)_{\mathrm{obs}}] \quad (2)$$

$$\Delta t = 21.8[\log(\mathrm{U}/\mathrm{Th})_0 - \log(\mathrm{U}/\mathrm{Th})_{\mathrm{obs}}] \quad (3)$$

where Δt is expressed in Gyr, r is a stable third-peak r-process element (here Os or Ir), and the terms such as $(\mathrm{Th}/r)_0$ are the initial production ratios for each pair of species.

Equations (1) and (2) highlight the importance of adding U to the battery of Galactic chronometers: an error of 0.1 dex in a Th abundance propagates as a time equal to the age of the Solar System, neglecting other sources of error. But equation (3) shows that U and Th can be used in concert, with little loss in formal precision but with important overall advantages: the initial production ratio $(\mathrm{U}/\mathrm{Th})_0$ is in principle much less affected[17] by theoretical uncertainties than any of the individual $(\mathrm{U}/r)_0$ because of the proximity of the two elements in their mass numbers. We note that the observational accuracy of (U/Th) is better than for U or Th alone, because errors coming from the choice of model atmosphere parameters largely cancel out.

The observed value of log(U/Th) in CS31082–001 is -0.74 ± 0.15. Here our error estimate includes 0.1 dex reflecting astrophysical observational errors, and 0.12 dex for the uncertainty on the oscillator strength of the U II 385.96-nm line. We only have to introduce an estimate of $\log(\mathrm{U}/\mathrm{Th})_0$ in equation (3) to derive the age of CS31082–001. This is done in Table 1, where we have given the reference used for the value of the production ratio. We have also explored the use of the ratio of U to stable elements. As explained above, it is safest to choose a reference element as heavy as possible (that is, close in mass number to U and Th). Table 1 gives the corresponding results using production ratios for Os and Ir from ref. 4. Any age between 11.1 and 13.9 Gyr is compatible with the various determinations associated with their error bars. We consider the median value 12.5 Gyr as our best present estimate for the age of CS31082–001, with a conservative standard error of 3 Gyr. When increased by 0.1–0.3 Gyr (refs 14, 15), these values give the age of the Galaxy, which is in turn a lower limit to the age of the Universe.

The accuracy of this uranium dating technique is at present limited by incomplete knowledge of a few critical physical data, in particular oscillator strengths and production ratios of the elements produced by the r-process. Further laboratory and theoretical work should enable progress on both these issues, as should the detection of additional stars with enhanced abundances of r-process elements, similar to CS31082–001. Such work, already in progress, should allow the full potential of the uranium chronometer to be realized. □

Table 1 Ages derived for CS31082–001 as a function of production ratios

Element pair	log (production ratio)	Ref.	log (observed ratio)	Derived age (Gyr)
U/Th	–0.255	4	–0.74 ± 0.15	10.6 ± 3.3
U/Th	–0.10	17	–0.74 ± 0.15	14.0 ± 3.3
U/Os	–1.27	4	–2.19 ± 0.18	13.6 ± 2.7
U/Ir	–1.30	4	–2.10 ± 0.17	11.8 ± 2.5

Received 9 November; accepted 29 December 2000.

1. Tilton, G. R. in *Meteorites and the Early Solar System* (eds Kerridge, J. F. & Matthews, M. S.) 249–258 (Univ. Arizona Press, Tucson, 1988).
2. Butcher, H. R. Thorium in G-dwarfs as a chronometer for the Galaxy. *Nature* **328,** 127–131 (1987).
3. François, P., Spite, M. & Spite, F. On the galactic age problem: Determination of the [Th/Eu] ratio in halo stars. *Astron. Astrophys.* **274,** 821–824 (1993).
4. Cowan, J. J. *et al.* *r*-process abundances and chronometers in metal-poor stars. *Astrophys. J.* **521,** 194–205 (1999).
5. Westin, J., Sneden, C., Gustafsson, B. & Cowan, J. J. The *r*-process enriched low-metallicity giant HD 115444. *Astrophys. J.* **530,** 783–799 (2000).
6. Sneden, C. *et al.* Evidence of multiple *r*-process sites in the early Galaxy: New observations of CS 22892-052. *Astrophys. J.* **533,** L139–L142 (2000).
7. Sneden, C. & Cowan, J. J. The age of the Galaxy from thorium cosmochronometry. *Rev. Mex. Astron. Astrophys.* (in the press); also preprint astro-ph/0008185 at ⟨http://xxx.lanl.gov⟩ (2000).
8. Beers, T. C., Preston, G. W. & Shectman, S. A. A search for stars of very low metal abundance. II. *Astron. J.* **103,** 1987–2034 (1992).
9. D'Odorico, S. *et al.* The performance of UVES, the echelle spectrograph for the ESO VLT, and highlights of the first observations of stars and quasars. *Proc. SPIE* **4005,** 121–130 (2000).
10. McWilliam, A., Preston, G. W., Sneden, C. & Searle, L. Spectroscopic analysis of 33 of the most metal-poor stars. II. *Astron. J.* **109,** 2757–2799 (1995).
11. Sneden, C. *et al.* The ultra-metal-poor, neutron-capture-rich giant star CS 22892-052. *Astrophys. J.* **467,** 819–840 (1996).
12. Blaise, J. & Wyart, J.-F. *Tables Internationales de Constantes Sélectionnées* Vol. 20, *Energy Levels and Atomic Spectra of the Actinides* (Univ. Pierre et Marie Curie, Paris, 1992).
13. Chen, H.-L. & Borzileri, C. Laser induced fluorescence studies of U II produced by photoionization of uranium. *J. Chem. Phys.* **74,** 6063–6069 (1981).
14. Argast, D., Samland, M., Gerhard, O. E. & Thielemann, F.-K. Metal-poor halo stars as tracers of ISM mixing processes during halo formation. *Astron. Astrophys.* **356,** 873–887 (2000).
15. Chiappini, C., Matteucci, F., Beers, T. C. & Nomoto, K. The earliest phases of Galaxy formation. *Astrophys. J.* **515,** 226–238 (2000).
16. Pfeiffer, B., Kratz, K. -L. & Thielemann, F.-K. Analysis of the solar-system *r*-process abundance pattern with the new ETFSI-Q mass formula. *Z. Phys. A* **357,** 235–238 (1997).
17. Goriely, S. & Clerbaux, B. Uncertainties in the Th cosmochronometry. *Astron. Astrophys.* **346,** 798–804 (1999).
18. Fouqué, P. *et al.* An absolute calibration of DENIS (Deep Near Infrared Southern Sky Survey). *Astron. Astrophys. Suppl.* **141,** 313–317 (2000).

Acknowledgements

We thank the ESO staff for assistance during the observations, J.-F. Wyart and L. Tchang-Brillet for helping us to obtain the best current atomic data for Th and U, and G. Simon for providing the unpublished infrared colours for CS 31082–001from the DENIS[18] survey. Partial financial support for this work was obtained from the US NSF (to T.C.B.), and from the Carlsberg Foundation and Julie Damms Studiefond (to J.A. and B.N.).

Correspondence should be addressed to R.C. (e-mail: Roger.Cayrel@obspm.fr).

Generic mechanism for generating a liquid–liquid phase transition

Giancarlo Franzese*, Gianpietro Malescio†, Anna Skibinsky*, Sergey V. Buldyrev* & H. Eugene Stanley*

* *Center for Polymer Studies and Department of Physics, Boston University, Boston, Massachusetts 02215, USA*

† *Dipartimento di Fisica, Università di Messina and Istituto Nazionale Fisica della Materia, 98166 Messina, Italy*

Recent experimental results[1] indicate that phosphorus—a single-component system—can have a high-density liquid (HDL) and a low-density liquid (LDL) phase. A first-order transition between two liquids of different densities[2] is consistent with experimental data for a variety of materials[3,4], including single-component systems such as water[5–8], silica[9] and carbon[10]. Molecular dynamics simulations of very specific models for supercooled water[2,11], liquid carbon[12] and supercooled silica[13] predict a LDL–HDL critical point, but a coherent and general interpretation of the LDL–HDL transition is lacking. Here we show that the presence of

a LDL and a HDL can be directly related to an interaction potential with an attractive part and two characteristic short-range repulsive distances. This kind of interaction is common to other single-component materials in the liquid state (in particular, liquid metals[2,14–21]), and such potentials are often used to describe systems that exhibit a density anomaly[2]. However, our results show that the LDL and HDL phases can occur in systems with no density anomaly. Our results therefore present an experimental challenge to uncover a liquid–liquid transition in systems like liquid metals, regardless of the presence of a density anomaly.

Several explanations have been developed to understand the liquid–liquid phase transition. For example, the two-liquid models[4] assume that liquids at high pressure are a mixture of two liquid phases whose relative concentration depends on external parameters. Other explanations for the liquid–liquid phase transition assume an anisotropic potential[2,11–13]. Here we shall see that liquid–liquid phase transition phenomena can arise solely from an isotropic pair interaction potential with two characteristic lengths.

For molecular liquid phosphorus P_4 (as for water), a tetrahedral open structure is favoured at low pressures P and low temperatures T, but a denser structure is favoured at high P and high T (refs 1, 6, 8). The existence of these two structures with different densities suggests a pair interaction with two characteristic distances. The first distance can be associated with the hard-core exclusion between two particles and the second distance with a weak repulsion (soft core), which can be overcome at large pressure. Here we will use a generic three-dimensional (3D) model composed of particles interacting through an isotropic soft-core pair potential. Such isotropic potentials can be regarded as resulting from an average over the angular part of more realistic potentials, and are often used as a first approximation to understand the qualitative behaviour of real systems[2,14–22]. For Ce and Cs, a potential with nearest-neighbour repulsion and a weak long-range attraction was proposed[15]. By means of an exact analysis in one dimension (1D), two critical points were found[15], with the high-density critical point interpreted as a solid–solid transition. Then analytic calculations[16], simulations[17] and the 1D exact solution (ref. 18) of the structure factor for a model with a soft-core potential were found to be consistent with experimental structure factors for liquid metals such as Bi. The structure factor for liquid metals was also the focus of a theoretical study of a family of soft-core potentials by mean-spherical approximation[19]. More recently, the analysis of the solid phase of a model with a soft-core potential[20] was related to the experimental evidence of a liquid–liquid critical point in the K_2Cs metallic alloy[21]. Moreover, for simple metals, soft-core potentials have been derived by first-principle calculations[14] and computed from experimental data[2]. Soft-core potentials are important in the context of supercooled liquids[23–25], and the analysis of experimental data for water gives rise to a soft-core potential[26].

The isotropic pair potential considered here (Fig. 1a, inset) has a hard-core radius a and a soft-core radius $b > a$. For $a < r < b$ the particles repel each other with energy $U_R > 0$; for $b < r < c$ they attract each other with energy $-U_A < 0$. For $r > c$ the interaction is considered negligible and is approximated to zero. The potential has three free parameters: b/a, c/a and U_R/U_A.

To select the parameters for the molecular dynamics (MD) simulations is not easy, and MD is too time-consuming to study a wide range of parameter values. Hence we first perform an integral equation analysis[27], whose predictions we can calculate very rapidly and efficiently. In this technique, one derives the phase diagram by studying the static pair distribution function—which measures the probability of finding a particle at a given distance from a reference particle, and thereby quantifies the correlation between pairs of particles. Mathematically, this function can be written as the sum of an infinite series of many-dimensional integrals, over particle coordinates, involving the pair interaction potential. Because this exact expression is intractable, approximations must be made. Here we use the hypernetted-chain approximation, which consists of neglecting a specific class of these integrals, leading to a simplified integral equation that can be solved numerically. In the temperature–density (T–ρ) phase diagram, the region where the simplified equation has no solutions is related[27] to the region where the system separates into two fluid phases. Thus this technique allows us to estimate the parameter range where two critical points occur, and hence to find useful parameter values for the MD simulations: $b/a = 2.0$, $c/a = 2.2$ and $U_R/U_A = 0.5$. We also use several additional parameter sets in the MD calculations.

Specifically, we perform MD simulations in 3D at constant volume V and number of particles $N = 490$ and 850. We use periodic boundary conditions, a standard collision event list

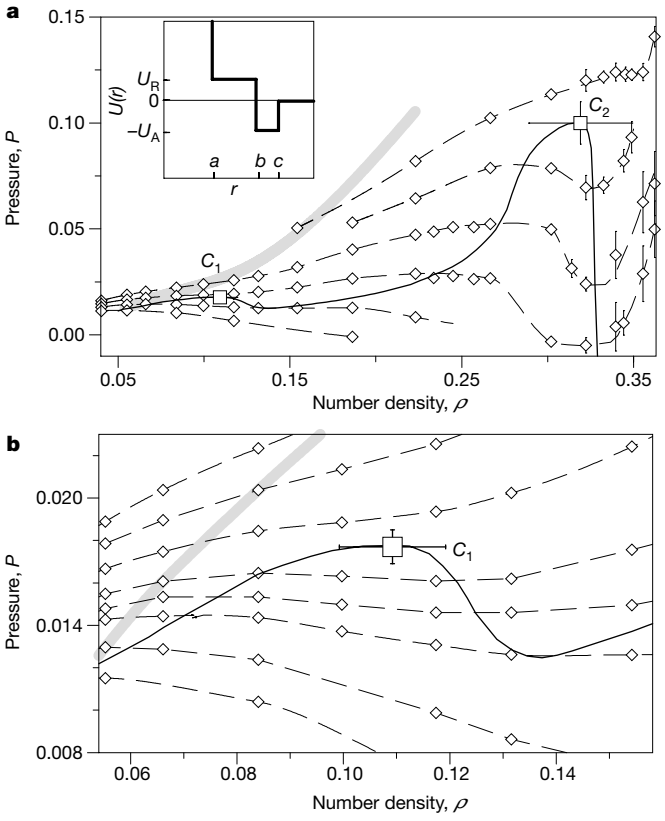

Figure 1 Pressure-density isotherms, crystallization line and spinodal line from the molecular dynamics simulations for the isotropic pair potential in three dimensions. Inset to **a**, the pair potential energy $U(r)$ as a function of the distance r between two particles. Distance a is the hard-core radius, b is the soft-core radius, c is the cut-off radius. Energy U_A is the attractive energy and U_R is the repulsive energy. **a**, Several isotherms (bottom to top) for $T = 0.57$, 0.59, 0.61, 0.63, 0.65 and 0.67. All quantities are in reduced units: length in units of a, temperature in units of U_A/k_B, pressure in units of U_A/a^3, (number) density in units of $1/a^3$. Diamonds represent data points and lines are guides for the eyes. The solid line connecting local maxima and minima along the isotherms represents the spinodal line. The two maxima of the spinodal line (squares) represent the two critical points C_1 and C_2. To determine the crystallization line (grey line)—below which the fluid is metastable with respect to the crystal—we place a crystal seed, prepared at very low T, in contact with the fluid, and check, for each (T,ρ) pair, whether the seed grows or melts after 10^6 MD steps. The spontaneous formation (nucleation) of the crystal is observed, within our simulation times ($\sim 10^5$ MD steps), only for $\rho \geq 0.27$. We use the structure factor $S(Q)$—the Fourier transform of the density–density correlation function for wave vectors Q—to determine when the nucleation occurs. Indeed, at the onset of nucleation, $S(Q)$ develops large peaks at finite Q ($Q = 12a^{-1}$ and $Q = 6a^{-1}$). For each ρ, we quench the system from a high-T configuration. After a transient time for the fluid equilibration, we compute $P(T,\rho)$, averaging more than 10^5–10^6 configurations generated from up to 12 independent quenches, making sure that the calculations are done before nucleation takes place. **b**, Enlarged view of the region around the gas–LDL critical point C_1 for $T = 0.570$, 0.580, 0.590, 0.595, 0.600, 0.610, 0.620 and 0.630.

algorithm[24], and a modified Berendsen method to control T (ref. 28). We find, for each set of parameters, the appearance of two critical points (Fig. 1).

A critical point is revealed by the presence of a region, in the pressure–density (P–ρ) phase diagram, with negative-slope isotherms. In MD simulations this region is related to the coexistence of two phases[2]. The (local) maximum and minimum along an isotherm correspond to the limits of stability of the existence of each single phase (supercooled and superheated phase, respectively). By definition, these maxima and minima are points on the spinodal line for that temperature. Because the spinodal line has a maximum at a critical point, one way to locate a critical point is to find this maximum. In our simulations (Fig. 1), we find two regions with negatively sloped isotherms and the overall shape of the spinodal line has two maxima, showing the presence of two critical points, C_1 and C_2. Using the Maxwell construction in the P–V plane[2], we evaluate the coexistence lines of the two fluid phases associated with each critical point (Fig. 2). Considering both the maxima of the spinodal line and the maxima of the coexistence regions in the P–ρ and P–T planes, we estimate the low-density critical point C_1 at $T_1 = 0.606 \pm 0.004$, $P_1 = 0.0177 \pm 0.0008$, $\rho_1 = 0.11 \pm 0.01$ and the high-density critical point C_2 at $T_2 = 0.665 \pm 0.005$, $P_2 = 0.10 \pm 0.01$, $\rho_2 = 0.32 \pm 0.03$. Temperatures are in units of U_A/k_B (where k_B is the Boltzmann constant), pressures in units of U_A/a^3, and (number) densities in units of $1/a^3$. Critical point C_1 is at the end of the phase-transition line separating the gas phase and the LDL phase, while critical point C_2 is at the end of the phase-transition line separating the gas phase and the HDL phase. Their relative positions resemble the phosphorus phase diagram, except that, in the experiments, C_2 has not been located[1], but is expected at the end of the gas–HDL transition line.

Our phase diagram (Fig. 2) shows the following fluid phases. At high $T > T_2$, the only fluid phase is the gas. At $T_1 < T < T_2$, we find—depending on ρ—the gas alone, or the HDL alone (turquoise region), or the HDL coexisting with gas (black line in Fig. 2a and green region in Fig. 2c). Below T_1, the LDL phase appears alone (blue region), or in coexistence with the HDL (orange line in Fig. 2b and orange region in Fig. 2d), or in coexistence with the gas (red line in Fig. 2b and red region in Fig. 2d). The point where the gas–LDL coexistence line merges with the LDL–HDL coexistence line is the triple point. Below the pressure and temperature of the triple point, the LDL is not stable and separates into gas and HDL.

For phosphorus the liquid–liquid transition occurs in the stable fluid regime[1]. In contrast, for our model, it occurs in the metastable fluid regime (see Fig. 1). We therefore wish to understand how to enhance the stability of the critical points with respect to the crystal phase. We find that by increasing the attractive well width $(c - b)/a$, both critical temperatures T_1 and T_2 increase, and hence both critical points move toward the stable fluid phase, analogous to results for attractive potentials with a single critical point[29,30]. For example, for attractive well width $(c - b)/a = 0.2$, both C_1 and C_2 are metastable with respect to the crystal, whereas for $(c - b)/a > 0.7$ we find C_1 in the stable fluid phase.

The phase diagram also depends sensitively on the relative width of the shoulder b/a and on its relative height U_R/U_A. By decreasing b/a or by increasing U_R/U_A, T_2 decreases and becomes smaller than T_1. This means that, in these cases, the high-density C_2 occurs below the temperature of the gas–liquid critical point, that is, C_2 is in the liquid phase and represents a LDL–HDL critical point, as in supercooled water[6,7,11].

The soft-core potential with the parameter sets we use displays no 'density anomaly' $(\partial V/\partial T)_P < 0$. This result is surprising at first because soft-core potentials have often been used to explain the density anomaly (see, for example refs 2 and 24). To understand this result, we consider the entropy S (the degree of disorder in the system) and the thermodynamic relation $-(\partial V/\partial T)_P = (\partial S/\partial P)_T = (\partial S/\partial V)_T(\partial V/\partial P)_T$. As, of necessity, $(\partial V/\partial P)_T < 0$, $(\partial V/\partial T)_P < 0$ implies $(\partial S/\partial V)_T < 0$, that is, the density anomaly implies that the disorder in the system increases for decreasing volume. For

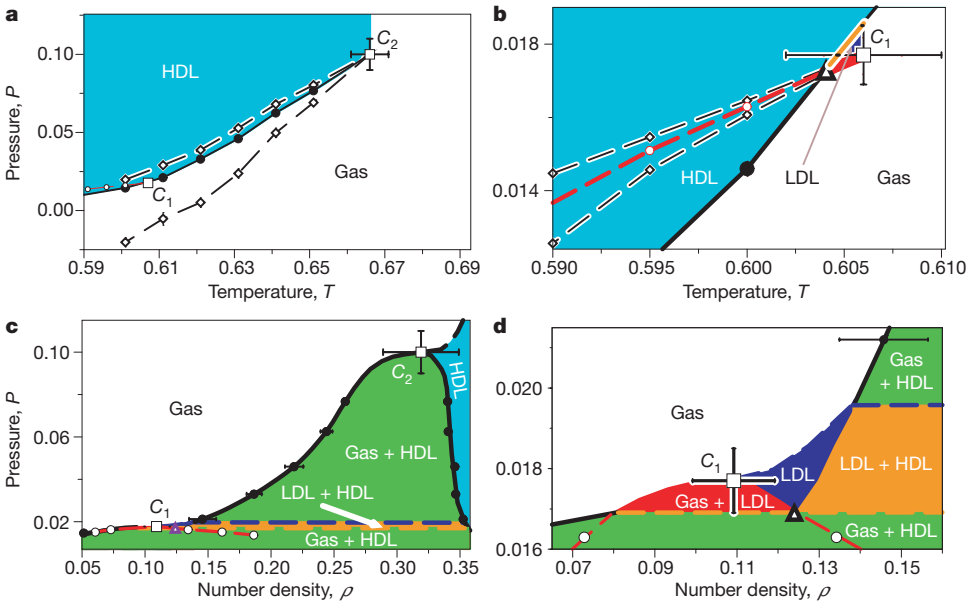

Figure 2 The phase diagrams, with coexistence lines and critical points resulting from MD simulations. **a**, **b**, P–T phase diagram. **b** is an enlargement of **a** in the vicinity of C_1. Circles represent points on the coexistence lines: open circles are for the gas–LDL coexistence, filled circles for the gas–HDL coexistence. Lines are guides for the eyes. The solid black line is the gas–HDL coexistence line. The red line is the gas–LDL coexistence line. The solid red line is stable, and the dashed red line is metastable, with respect to the HDL phase. The orange line is the LDL–HDL coexistence line. The triangle represents the triple point. The projection of the spinodal line is represented in **a** and **b** by diamonds with dashed lines. The spinodal line is folded in this projection, with two cusps corresponding to the two maxima in Fig. 1. Critical points occur where the coexistence lines meet these cusps. The critical point C_1 is for the gas–LDL transition, and C_2 is for the gas–HDL transition. **c**, **d**, P–ρ projections of **a** and **b**. The colours, symbols and patterns of coexistence lines, triple and critical points are the same as in **a** and **b**. Dashed blue, black and orange lines schematically represent isotherms at the temperatures of C_1, C_2 and of the triple point, respectively. Both gas–LDL and gas–HDL coexistence lines show a local maximum, representing the estimates of C_1 and C_2, respectively. In all the panels, where not shown, the errors are smaller than the symbol size. Units of P, T and ρ are as in Fig. 1.

example, this is the case for water. This is consistent with the negative slope dP/dT of the crystal–liquid transition line for water, that implies that $\Delta S/\Delta V < 0$ since, according to the Clausius–Clapeyron equation, $dP/dT = \Delta S/\Delta V$, where ΔS and ΔV are the entropy and volume differences between the two coexisting phases.

For our system, we expect the reverse: $(\partial V/\partial T)_P > 0$ so $(\partial S/\partial V)_T > 0$, consistent with the positive slope of the LDL–HDL transition line dP/dT (see Fig. 2b). We confirm that $(\partial S/\partial V)_T > 0$ by explicitly calculating S for our system by means of thermodynamic integration.

Our results show that the presence of two critical points and the occurrence of the density anomaly are not necessarily related, suggesting that we might seek experimental evidence of a liquid–liquid phase transition in systems with no density anomaly. In particular, a second critical point may also exist in liquid metals that can be described by soft-core potentials. Thus the class of experimental systems displaying a second critical point may be broader than previously hypothesized. □

Received 6 October; accepted 18 December 2000.

1. Katayam, Y. *et al.* A first-order liquid–liquid phase transition in phosphorus. *Nature* **403,** 170–173 (2000).
2. Debenedetti, P. G. *Metastable Liquids: Concepts and Principles* (Princeton Univ. Press, Princeton, 1998).
3. Wilding, M. C., McMillan, P. F. & Navrotsky, A. The thermodynamic nature of a phase transition in yttria-alumina liquids. *J. Cryst. Noncryst. Solids* (in the press).
4. Brazhkin, V. V., Popova, S. V. & Voloshin, R. N. High-pressure transformations in simple melts. *High Pressure Res.* **15,** 267–305 (1997).
5. Brazhkin, V. V., Gromnitskaya, E. L., Stalgorova, O. V. & Lyapin, A. G. Elastic softening of amorphous H_2O network prior to the *HDA–LDA* transition in amorphous state. *Rev. High Pressure Sci. Technol.* **7,** 1129–1131 (1998).
6. Mishima, O. Liquid–liquid critical point in heavy water. *Phys. Rev. Lett.* **85,** 334–336 (2000).
7. Bellissent-Funel, M.-C. Evidence of a possible liquid–liquid phase transition in super-cooled water by neutron diffraction. *Nuovo Cimento* **20D,** 2107–2122 (1998).
8. Soper, A. K. & Ricci, M. A. Structures of high-density and low-density water. *Phys. Rev. Lett.* **84,** 2881–2884 (2000).
9. Lacks, D. J. First-order amorphous-amorphous transformation in silica. *Phys. Rev. Lett.* **84,** 4629–4632 (2000).
10. van Thiel, M. & Ree, F. H. High-pressure liquid–liquid phase change in carbon. *Phys. Rev. B* **48,** 3591–3599 (1993).
11. Poole, P. H., Sciortino, F., Essmann, U. & Stanley, H. E. Phase behavior of metastable water. *Nature* **360,** 324–328 (1992).
12. Glosli, J. N. & Ree, F. H. Liquid–liquid phase transformation in carbon. *Phys. Rev. Lett.* **82,** 4659–4662 (1999).
13. Saika-Voivod, I., Sciortino, F. & Poole, P. H. Computer simulations of liquid silica: Equation of state and liquid–liquid phase transition. *Phys. Rev. E* **63,** 011202-1–011202-9 (2001).
14. Mon, K. K., Ashcroft, M. W. & Chester, G. V. Core polarization and the structure of simple metals. *Phys. Rev. B* **19,** 5103–5118 (1979).
15. Stell, G. & Hemmer, P. C. Phase transition due to softness of the potential core. *J. Chem. Phys.* **56,** 4274–4286 (1972).
16. Silbert, M. & Young, W. H. Liquid metals with structure factor shoulders. *Phys. Lett.* **58A,** 469–470 (1976).
17. Levesque, D. & Weis, J. J. Structure factor of a system with shouldered hard sphere potential. *Phys. Lett.* **60A,** 473–474 (1977).
18. Kincaid, J. M. & Stell, G. Structure factor of a one-dimensional shouldered hard-sphere fluid. *Phys. Lett.* **65A,** 131–134 (1978).
19. Cummings, P. T. & Stell, G. Mean spherical approximation for a model liquid metal potential. *Mol. Phys.* **43,** 1267–1291 (1981).
20. Velasco, E., Mederos, L., Navascués, G., Hemmer, P. C. & Stell, G. Complex phase behavior induced by repulsive interactions. *Phys. Rev. Lett.* **85,** 122–125 (2000).
21. Voronel, A., Paperno, I., Rabinovich, S. & Lapina, E. New critical point at the vicinity of freezing temperature of K_2Cs. *Phys. Rev. Lett.* **50,** 247–249 (1983).
22. Behrens, S. H., Christl, D. I., Emmerzael, R., Schurtenberger, P. & Borkovec, M. Charging and aggregation properties of carboxyl latex particles: Experiments versus DLVO theory. *Langmuir* **16,** 2566–2575 (2000).
23. Debenedetti, P. G., Raghavan, V. S. & Borick, S. S. Spinodal curve of some supercooled liquids. *J. Phys. Chem.* **95,** 4540–4551 (1991).
24. Sadr-Lahijany, M. R., Scala, A., Buldyrev, S. V. & Stanley, H. E. Liquid state anomalies for the Stell-Hemmer core-softened potential. *Phys. Rev. Lett.* **81,** 4895–4898 (1998).
25. Jagla, E. A. Core-softened potentials and the anomalous properties of water. *J. Chem. Phys.* **111,** 8980–8986 (1999).
26. Stillinger, F. H. & Head-Gordon, T. Perturbational view of inherent structures in water. *Phys. Rev. E* **47,** 2484–2490 (1993).
27. Caccamo, C. Integral equation theory description of phase equilibria in classical fluids. *Phys. Rep.* **274,** 1–105 (1996).
28. Berendsen, H. J. C., Postma, J. P. M., van Gunsteren, W. F., DiNola, A. & Haak, J. R. Molecular dynamics with coupling to an external bath. *J. Chem. Phys.* **81,** 3684–3690 (1984).
29. Rein ten Wolde, P. & Frenkel, D. Enhancement of protein crystal nucleation by critical density fluctuations. *Science* **277,** 1975–1978 (1997).
30. Hagen, M. H. J., Meijer, E. J., Mooij, G. C. A. M., Frenkel, D. & Lekkerkerker, H. N. W. Does C_{60} have a liquid phase? *Nature* **365,** 425–426 (1993).

Acknowledgements

We wish to thank L. A. N. Amaral, P. V. Giaquinta, E. La Nave, T. Lopez Ciudad, S. Mossa, G. Pellicane, A. Scala, F. W. Starr, J. Teixeira, and, in particular, F. Sciortino for helpful suggestions and discussions. We thank the NSF and the CNR (Italy) for partial support.

Correspondence and requests for materials should be addressed to G.F. (e-mail: franzese@argento.bu.edu).

Strong radiative heating due to the mixing state of black carbon in atmospheric aerosols

Mark Z. Jacobson

Department of Civil & Environmental Engineering, Stanford University, Stanford, California 94305-4020, USA

Aerosols affect the Earth's temperature and climate by altering the radiative properties of the atmosphere. A large positive component of this radiative forcing from aerosols is due to black carbon—soot—that is released from the burning of fossil fuel and biomass, and, to a lesser extent, natural fires, but the exact forcing is affected by how black carbon is mixed with other aerosol constituents. From studies of aerosol radiative forcing, it is known that black carbon can exist in one of several possible mixing states; distinct from other aerosol particles (externally mixed[1–7]) or incorporated within them (internally mixed[1,3,7]), or a black-carbon core could be surrounded by a well mixed shell[7]. But so far it has been assumed that aerosols exist predominantly as an external mixture. Here I simulate the evolution of the chemical composition of aerosols, finding that the mixing state and direct forcing of the black-carbon component approach those of an internal mixture, largely due to coagulation and growth of aerosol particles. This finding implies a higher positive forcing from black carbon than previously thought, suggesting that the warming effect from black carbon may nearly balance the net cooling effect of other anthropogenic aerosol constituents. The magnitude of the direct radiative forcing from black carbon itself exceeds that due to CH_4, suggesting that black carbon may be the second most important component of global warming after CO_2 in terms of direct forcing.

This work was motivated by studies[1–7] that found different black-carbon (BC) forcings when different BC mixing states were assumed. In one study[7] the mixing state was found to affect the BC global direct forcing by a factor of 2.9 (0.27 $W m^{-2}$ for an external mixture, +0.54 $W m^{-2}$ for BC as a coated core, and +0.78 $W m^{-2}$ for BC as well mixed internally). Because BC is a solid and cannot physically be well mixed in a particle, the third case was discarded as unrealistic, and it was suggested that the real forcing by BC probably fell between that from an external mixture and that from a coated core. Here I report simulations that were performed among multiple aerosol size distributions to estimate which of these two treatments, if either, better approximates BC forcing in the real atmosphere.

The global model that I used was GATOR-GCMM, which treated gas, aerosol, radiative, meteorological and transport processes (see Supplementary Information for details). Aerosol processes included emissions, homogeneous nucleation, condensation, dissolution, coagulation, chemical equilibrium, transport, sedimentation, dry deposition, and rainout among 18 aerosol size distributions, 17 size bins per distribution, one number concentration, and an average of seven mole concentrations per bin per distribution. The 18 distributions (Supplementary Information) consisted of four 'primary' size distributions (sea spray (A), soil (B), black carbon (E1) and organic